bioRxiv preprint doi: https://doi.org/10.1101/073585; this version posted September 5, 2016. The copyright holder for this preprint (which was not certified by peer review) is the author/funder, who has granted bioRxiv a license to display the preprint in perpetuity. It is made available under aCC-BY-NC-ND 4.0 International license.

Measuring MEG closer to the brain: Performance of on-scalp sensor arrays

Joonas Iivanainen[a,*], Matti Stenroos[a], Lauri Parkkonen[a,b]

[a]*Department of Neuroscience and Biomedical Engineering, Aalto University School of Science, FI-00076 AALTO, Finland*
[b]*Aalto NeuroImaging, Aalto University, FI-00076 AALTO, FINLAND*

Abstract

Optically-pumped magnetometers (OPMs) have recently reached sensitivity levels required for magnetoencephalography (MEG). OPMs do not need cryogenics and can thus be placed within millimetres from the scalp into an array that adapts to the invidual head size and shape, thereby reducing the distance from cortical sources to the sensors. Here, we quantified the improvement in recording MEG with hypothetical on-scalp OPM arrays compared to a 306-channel state-of-the-art SQUID array (102 magnetometers and 204 planar gradiometers).

We simulated OPM arrays that measured either normal (nOPM; 102 sensors), tangential (tOPM; 204 sensors), or all components (aOPM; 306 sensors) of the magnetic field. We built forward models based on magnetic resonance images of 10 adult heads; we employed a three-compartment boundary element model and distributed current dipoles evenly across the cortical mantle.

Compared to the SQUID magnetometers, nOPM and tOPM yielded 7.5 and 5.3 times higher signal power, while the correlations between the field patterns of source dipoles were reduced by factors of 2.8 and 3.6, respectively. Values of the field-pattern correlations were similar across nOPM, tOPM and SQUID gradiometers. The information capacities of the OPM arrays were clearly higher than that of the SQUID array. The dipole-localization accuracies of the arrays were similar while the minimum-norm-based point-spread functions were on average 2.4 and 2.5 times more spread for the SQUID array compared to nOPM and tOPM arrays, respectively.

The results indicate that on-scalp MEG arrays offer clear benefits over a traditional SQUID array in several aspects of performance.

Keywords: magnetoencephalography, lead field, superconducting quantum interference device, optically-pumped magnetometer, atomic magnetometer, sensor array

1. Introduction

Magnetoencephalography (MEG) is a non-invasive neuroimaging technique that detects the magnetic fields of electrically active neuron populations in the human brain (Hämäläinen et al.,

*Corresponding author at: Department of Neuroscience and Biomedical Engineering, Aalto University School of Science, FI-00076 AALTO, Finland

Email address: joonas.iivanainen@aalto.fi (Joonas Iivanainen)

bioRxiv preprint doi: https://doi.org/10.1101/073585; this version posted September 5, 2016. The copyright holder for this preprint (which was not certified by peer review) is the author/funder, who has granted bioRxiv a license to display the preprint in perpetuity. It is made available under aCC-BY-NC-ND 4.0 International license.

1993). Due to the weakness of these fields, highly sensitive detectors (magnetometers) are needed. Until recently, superconducting quantum interference devices (SQUIDs) have been the only sensors with adequate sensitivity to enable practical mapping of the cerebral neuromagnetic fields. However, SQUIDs require a cryogenic environment, and liquid helium (boiling point 4.2 K) is typically used for reaching sufficiently low temperatures. The necessity of cryogenics imposes several problems: First, cryogenics make MEG systems bulky. Second, the necessary thermal isolation between the sensors and the subject sets a lower limit, typically about 2 cm, on the distance from the sensors to the scalp of the subject. Last, a SQUID-based sensor array is not adjustable to individual head size and shape, which further increases the average distance between sensors and scalp. Alternative sensors such as optically-pumped, or atomic, magnetometers (OPMs) (Budker and Kimball, 2013; Budker and Romalis, 2007) and high-T_c SQUIDs (Öisjöen et al., 2012) have recently reached sensitivities required for detecting neuromagnetic fields.

Particularly OPMs operating in the spin-exchange relaxation-free (SERF) regime (Allred et al., 2002) could become a feasible, non-cryogenic alternative to SQUIDs for neuromagnetic measurements as the dimensions and sensitivies of the SERF-OPMs are approaching those of SQUIDs ($\sim$cm^2 and $\sim$3 fT/$\sqrt{\text{Hz}}$). Johnson and colleagues (2010) reported that they achieved a sensitivity better than 5 fT/$\sqrt{\text{Hz}}$ with their SERF-OPM with a footprint of 6×6 cm^2. A smaller chip-scale microfabricated OPM developed by Mhaskar and colleagues (2012) has a volume of about (1 cm)^3 and sensitivity better than 20 fT/$\sqrt{\text{Hz}}$. Shah and Wakai (2013) have demonstrated an OPM with a volume of $2\times2\times5$ cm^3 and sensitivity of 10 fT/$\sqrt{\text{Hz}}$ during a field study and 6 fT/$\sqrt{\text{Hz}}$ in the laboratory; the theoretical photon-shot-noise-limited sensitivity of that OPM was 1 fT/$\sqrt{\text{Hz}}$.

The sensitivies of the OPMs should thus allow the measurement of weak neuromagnetic fields, while their dimensions enable multichannel whole-head-covering measurements. OPMs could also be placed within few millimetres from scalp, permitting EEG-cap-like MEG arrays. Here, we compare the performance of such on-scalp MEG sensor arrays against conventional SQUID arrays.

We simulate the performance of hypothetical on-scalp OPM arrays of sensors that measure the normal and tangential components of the neuromagnetic field. We compare the performance of such arrays to a state-of-the-art SQUID-based 306-channel MEG array. In our simulations, we use realistic geometries derived from magnetic resonance images of ten adult subjects and calculate magnetic fields using the boundary element method. Our aim is to examine the possible benefits that result from recording MEG closer to the brain and to investigate differences in the measurements of normal and tangential components of the magnetic field. We use both novel and well-established metrics derived from forward models and point-spread functions of the minimum-norm estimates. The metrics quantify signal power, information, similarity of the field patterns of the sources, overlap of the sensor lead-fields, localization accuracy and resolution. Besides measures of performance evaluation, such metrics can be used to guide the design of MEG sensor arrays. In addition, we quantify the differences in the measurements of normal and tangential field components by analyzing the contributions they receive from primary and secondary currents.

2. Theory

In this section, we shortly review the key physics and introduce the concepts used in the forward and inverse modeling employed in this study.

bioRxiv preprint doi: https://doi.org/10.1101/073585; this version posted September 5, 2016. The copyright holder for this preprint (which was not certified by peer review) is the author/funder, who has granted bioRxiv a license to display the preprint in perpetuity. It is made available under aCC-BY-NC-ND 4.0 International license.

2.1. Physics

When bioelectromagnetic fields are modeled in the macroscopic scale, the time-dependent terms in Maxwell's equations can be omitted (Plonsey and Heppner, 1967). The total current density in the head is divided into two parts; $\mathbf{J} = \mathbf{J}_\mathrm{p} + \mathbf{J}_\mathrm{V}$, where $\mathbf{J}_\mathrm{p}$ is the primary current density representing the neuronal source activity while $\mathbf{J}_\mathrm{V}$ is the volume current density, which is driven by the electric field caused by $\mathbf{J}_\mathrm{p}$ and is present everywhere in the conductor. The electric potential ϕ is then given by $\nabla \cdot (\sigma \nabla \phi) = \nabla \cdot \mathbf{J}_\mathrm{p}$, where σ is conductivity, and the magnetic field can be obtained by integrating the total current using Biot–Savart law. When the conducting region is modeled to consist of piecewise homogeneous regions, the magnetic field is given by the Geselowitz formula; (Geselowitz, 1970)

$$\begin{aligned} \mathbf{B}(\mathbf{r}) &= \mathbf{B}_\mathrm{p}(\mathbf{r}) + \mathbf{B}_\mathrm{v}(\mathbf{r}) && (1) \\ &= \frac{\mu_0}{4\pi} \int_V \frac{\mathbf{J}_\mathrm{p}(\mathbf{r}') \times (\mathbf{r} - \mathbf{r}')}{|\mathbf{r} - \mathbf{r}'|^3} \mathrm{d}V' \\ &\quad + \frac{\mu_0}{4\pi} \sum_{k=1}^{N} (\sigma_\mathrm{in}^k - \sigma_\mathrm{out}^k) \int_{S^k} \phi(\mathbf{r}') \frac{(\mathbf{r} - \mathbf{r}')}{|\mathbf{r} - \mathbf{r}'|^3} \times \mathrm{d}\mathbf{S}', && (2) \end{aligned}$$

where $\mathbf{B}_\mathrm{p}(\mathbf{r})$ and $\mathbf{B}_\mathrm{v}(\mathbf{r})$ are the magnetic fields due to primary and volume currents, μ_0 is the permeability of free space, and σ_in^k and σ_out^k are the conductivities inside and outside the kth surface S^k, respectively. The magnetic field can thus be obtained by first solving for the potential on conductivity boundaries and then integrating. Boundary element method (BEM) is a convenient choice for computing the potential and magnetic field in a piecewise homogeneous volume conductor (e.g. Stenroos et al. (2007)).

2.2. Forward model

The primary current distribution is typically discretized into a set of current dipoles (Hämäläinen et al., 1993). The output of a sensor is obtained by integrating the magnetic field due to primary-current dipoles through the sensitive volume of the sensor; the sensitive volume is discretized into a set of integration points and the integral is approximated by a weighted sum of the magnetic field components at these points.

With these models, the magnetic-field amplitudes at the N_c sensors $\mathbf{b} \in \mathscr{R}^{N_c \times 1}$ are related to the N_s amplitudes of the current dipoles $\mathbf{j} \in \mathscr{R}^{N_s \times 1}$ by a linear mapping

$$\mathbf{b} = \mathbf{L}\mathbf{j}, \tag{3}$$

where $\mathbf{L} \in \mathscr{R}^{N_c \times N_s}$ is the lead-field matrix. The ith column of the lead-field matrix ($\mathbf{t}_i$) represents the magnetic field pattern (topography) of the ith unit dipole (source); the jth row ($\mathbf{l}_j$) represents the sensitivity pattern of sensor j to the current dipoles, i.e., the lead field of sensor j. According to the Geselowitz formula presented earlier, the lead-field matrix can be considered a sum of two matrices:

$$\mathbf{L} = \mathbf{P} + \mathbf{V}, \tag{4}$$

where $\mathbf{P}$ and $\mathbf{V}$ represent the contributions of the primary and volume currents, respectively.

bioRxiv preprint doi: https://doi.org/10.1101/073585; this version posted September 5, 2016. The copyright holder for this preprint (which was not certified by peer review) is the author/funder, who has granted bioRxiv a license to display the preprint in perpetuity. It is made available under aCC-BY-NC-ND 4.0 International license.

2.3. *Minimum-norm estimate*

Minimum-l_2-norm estimator (Dale and Sereno, 1993; Hämäläinen and Ilmoniemi, 1994) can be used to estimate underlying sources from measured data. The source estimate, which satisfies the regularized minimum-l_2-norm condition and takes into account the spatiotemporal properties of the noise, is

$$\tilde{\mathbf{j}} = \mathbf{L}^T(\mathbf{L}\mathbf{L}^T + \lambda^2\mathbf{C})^{-1}\mathbf{b} \equiv \mathbf{G}\mathbf{b}, \tag{5}$$

where λ^2 is the regularization parameter, $\mathbf{C}$ is the noise covariance matrix and $\mathbf{G}$ is the minimum-norm estimator. The regularization parameter has been suggested to be chosen as (Lin et al., 2006a,b)

$$\lambda^2 = \frac{\mathrm{tr}(\tilde{\mathbf{L}}\tilde{\mathbf{L}}^T)}{N_c \mathrm{SNR}}, \tag{6}$$

where N_c is the number of sensors, SNR is the estimated signal-to-noise ratio, $\mathrm{tr}(\cdot)$ is trace of a matrix and $\tilde{\mathbf{L}}$ is the whitened lead-field matrix: $\tilde{\mathbf{L}} = \mathbf{C}^{-1/2}\mathbf{L}$.

3. Methods

Here, we present the methods and models that were used in the simulations and review the measures that we used to quantify the performance of the arrays. First, we constructed the anatomical models from the magnetic resonance images (MRIs), modeled the sensors and sensor arrays, and then computed the lead-field matrices. Prior to the actual simulations, we quantified whether the lead-field matrices of the OPM arrays are more sensitive to the skull-conductivity value and to the densities of BEM surface tessellations than the SQUID arrays. Subsequently, we built the lead-field matrices and minimum-norm estimators for the computation of performance metrics.

3.1. *Anatomical models*

T1-weighted MRIs were obtained from ten healthy adults (seven males, three females) using a 3-T scanner and a 3D MP-RAGE sequence. FreeSurfer software (Dale et al., 1999; Fischl et al., 1999a; Fischl, 2012) was used to segment the cortical mantles from individual MRIs. The primary current distributions were assumed to lie on the cortical surfaces and were discretized to sets of dipoles oriented normal to the local cortical surface (10 242 dipoles per hemisphere). For each subject, we used the watershed algorithm (Ségonne et al., 2004) implemented in FreeSurfer and MNE software (Gramfort et al., 2014) to segment the brain, skull and scalp compartments. We triangulated and decimated these surfaces to obtain three meshes (2 562 vertices per mesh) for the BEM. To estimate errors due to the coarser meshes, we constructed an additional model for one subject with surfaces comprising 10 242 vertices.

To obtain group-level metrics, the spherical morphing procedure in Freesurfer (Fischl et al., 1999b) was used to map the values from individual subjects to their average brain, where the values were subsequently averaged.

3.2. *Sensor models*

The sensor output was computed by integrating over a set of points within the sensing volume (OPMs) or pick-up coil plane (SQUIDs). The descriptions of the sensor geometries are presented in Table 1. The OPM sensor was a cube with a sidelength of 5 mm, and the integration points were distributed uniformly within that volume. The SQUID sensors were modeled as in the

bioRxiv preprint doi: https://doi.org/10.1101/073585; this version posted September 5, 2016. The copyright holder for this preprint (which was not certified by peer review) is the author/funder, who has granted bioRxiv a license to display the preprint in perpetuity. It is made available under aCC-BY-NC-ND 4.0 International license.

MNE software (Table 1; Gramfort et al. 2014). The OPMs were assumed to have a noise level of 6 fT/ $\sqrt{\text{Hz}}$ while the noise levels of SQUID magnetometers and gradiometers were 3 fT/ $\sqrt{\text{Hz}}$ and 3 fT/(cm $\sqrt{\text{Hz}}$), respectively.

Table 1: Sensor models used in this study. N is the number of integration points $\mathbf{r}$, w is the weight of each point and σ is the noise level.

Sensor type	N	$\mathbf{r}(x,y,z)$ [mm]	w	σ
OPM	8	($\pm$1.25, $\pm$1.25, 1.25)	1/8	6 fT/ $\sqrt{\text{Hz}}$
		($\pm$1.25, $\pm$1.25, 3.75)	1/8	
SQUID gradiometer	2	($\pm$8.4, 0, 0.3)	$\pm$1/16.8 mm	3 fT/(cm $\sqrt{\text{Hz}}$)
SQUID magnetometer	4	($\pm$6.45, $\pm$6.45, 0.3)	1/4	3 fT/ $\sqrt{\text{Hz}}$

3.3. Sensor arrays

The SQUID sensor arrays of the Elekta Neuromag® MEG system (102 magnetometers; 204 planar gradiometers; Elekta Oy, Helsinki, Finland) were positioned around the subjects' heads as in a real MEG measurement. For each subject, the position was optimized for good coverage of the entire cortex as well as for symmetry along the left–right axis. Thereafter, the sensor positions were verified to be at least 2 cm (approximate thickness of the MEG dewar) from the scalp. The SQUID array for each subject is shown in Fig. 1. We considered three variants of this array: planar gradiometers only (gSQUID), magnetometers only (mSQUID), and the full 306-channel array (aSQUID) with both sensor types.

The OPM locations (shown in Fig. 1) were derived from the SQUID arrays by projecting the sensor locations to the scalp. The distance of the closest face of the OPM sensor cube to scalp was set to 1 mm. For these positions, we defined three different OPM arrays: one with 102 sensors measuring the normal component of the magnetic field with respect to the local surface of the scalp (nOPM), other with 204 sensors measuring the two orthogonal tangential components (tOPM) and a combination of the aforementioned arrays, with 306 sensors measuring all field components (aOPM).

3.4. Forward models

For each subject, the lead-field matrix $\mathbf{L}$ was computed using a linear Galerkin BEM formulated with Isolated Source Approach (ISA) (Stenroos and Sarvas, 2012). The conductivities of the brain, skull and scalp compartments of the BEM model were set to [1 1/25 1]$\times$0.33 S/m. To assess the sensitivity of the calculated lead-field matrices to skull conductivity, in one subject we compared the computed topographies against those obtained with skull conductivity values of 0.33/50 and 0.33/80 S/m.

3.5. Minimum-norm estimator

We estimated the SNR in the regularization parameter of Eq. (6) with the average SNR of the cortical sources; we defined the SNR of source i as

$$\text{SNR}_i = \frac{q^2}{N_c}\text{tr}(\tilde{\mathbf{t}}_i\tilde{\mathbf{t}}_i^T), \tag{7}$$

where q^2 is the source variance and $\tilde{\mathbf{t}}_i = (\mathbf{C}^{-1/2}\mathbf{L})_i$ is the whitened topography of the ith source. We took into account only sensor noise which was assumed to be uncorrelated across the sensors;

bioRxiv preprint doi: https://doi.org/10.1101/073585; this version posted September 5, 2016. The copyright holder for this preprint (which was not certified by peer review) is the author/funder, who has granted bioRxiv a license to display the preprint in perpetuity. It is made available under aCC-BY-NC-ND 4.0 International license.

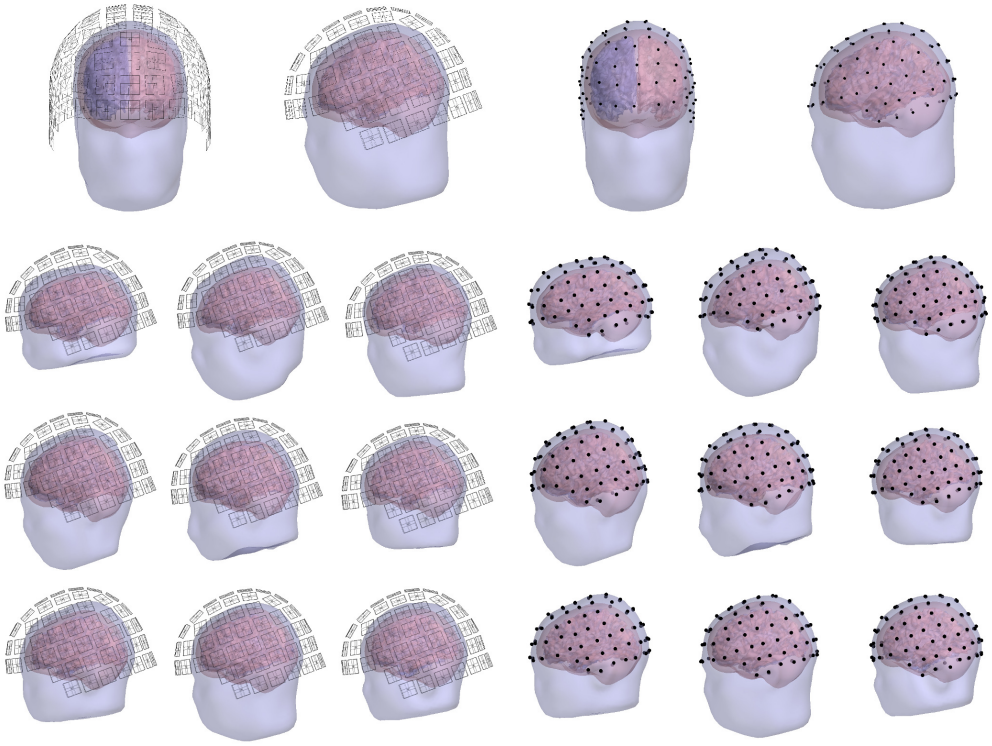

Figure 1: The constructed SQUID (left) and OPM (right) sensor positions. Top: Frontal and lateral views of the sensor locations for one subject. Other rows: Lateral views for the rest of the subjects.

bioRxiv preprint doi: https://doi.org/10.1101/073585; this version posted September 5, 2016. The copyright holder for this preprint (which was not certified by peer review) is the author/funder, who has granted bioRxiv a license to display the preprint in perpetuity. It is made available under aCC-BY-NC-ND 4.0 International license.

thus, we used a diagonal noise covariance matrix $\mathbf{C}$, whose diagonal elements were the noise variances σ_k^2 of the sensors. With a diagonal $\mathbf{C}$, Eq. (7) simplifies into (Goldenholz et al., 2009)

$$\mathrm{SNR}_i = \frac{q^2}{N_c} \sum_{k=1}^{N_c} \frac{t_{i,k}^2}{\sigma_k^2}. \tag{8}$$

We set the source variance q^2 so that the average SNR across the sources was 1 for the SQUID magnetometers and calculated the average SNRs and regularization parameters for the other arrays using that particular source variance.

3.6. Metrics

We analyzed the modeling errors with specific error measures. We computed topography power of the arrays and analyzed the contributions of the primary and volume currents to the signals. We then assessed the correlations between source topographies and examined the lead fields of the sensors by comparing the fields-of-view (FOVs) of the sensors and calculating correlations among the lead fields. To complete forward model -based metrics and quantify the performance of the array with a single number, we calculated the total information conveyed by the array (Kemppainen and Ilmoniemi, 1989). Last, we investigated the PSFs of the arrays in the minimum-norm estimation. We calculated all metrics individually for each subject, morphed the results to the average brain and averaged.

Error measures. To assess the numerical errors, we investigated the differences between the obtained topographies using metrics sensitive to differences in amplitudes and shapes of topographies. Relative error (RE) is such a measure, and for the ith source it is given by

$$\mathrm{RE}_i = \frac{\|\mathbf{t}_i^{\mathrm{ref}} - \mathbf{t}_i^{\mathrm{test}}\|}{\|\mathbf{t}_i^{\mathrm{ref}}\|}, \tag{9}$$

where $\mathbf{t}_i^{\mathrm{ref}}$ and $\mathbf{t}_i^{\mathrm{test}}$ are the test and reference topographies of the ith source and $\|\cdot\|$ is the l_2-norm. Correlation coefficient (CC) is sensitive only to differences in the field shape and is expressed for the ith source as

$$\mathrm{CC}_i = \frac{\mathbf{t}_i^{\mathrm{ref}} - \bar{\mathbf{t}}_i^{\mathrm{ref}}}{\|\mathbf{t}_i^{\mathrm{ref}} - \bar{\mathbf{t}}_i^{\mathrm{ref}}\|} \cdot \frac{\mathbf{t}_i^{\mathrm{test}} - \bar{\mathbf{t}}_i^{\mathrm{test}}}{\|\mathbf{t}_i^{\mathrm{test}} - \bar{\mathbf{t}}_i^{\mathrm{test}}\|}, \tag{10}$$

where $\cdot$ is the dot product and $\bar{\mathbf{t}}_i$ denotes the mean of $\mathbf{t}_i$.

Relative sensitivity. To compare the overall signal power of the arrays, we defined relative sensitivity

$$S_i^{a,b} = \frac{\|\mathbf{t}_i^a\|^2}{\|\mathbf{t}_i^b\|^2}, \tag{11}$$

where $\|\mathbf{t}_i^a\|^2$ and $\|\mathbf{t}_i^b\|^2$ are the topography power of the source i in arrays a and b, respectively. The relative sensitivity is related to the ratio of SNRs between arrays: if we assume that all sensors in the array have equal sensor noise variance σ^2, Eq. (7) simplifies to

$$\mathrm{SNR}_i = \frac{q^2}{N_c \sigma^2} \|\mathbf{t}_i\|^2. \tag{12}$$

Consequently, the ratio of SNRs of arrays a and b for source i is

$$\frac{\mathrm{SNR}_{i,a}}{\mathrm{SNR}_{i,b}} = \frac{N_{c,b}\sigma_b^2}{N_{c,a}\sigma_a^2} \frac{\|\mathbf{t}_i^a\|^2}{\|\mathbf{t}_i^b\|^2} = \frac{N_{c,b}\sigma_b^2}{N_{c,a}\sigma_a^2} S_i^{a,b}. \tag{13}$$

bioRxiv preprint doi: https://doi.org/10.1101/073585; this version posted September 5, 2016. The copyright holder for this preprint (which was not certified by peer review) is the author/funder, who has granted bioRxiv a license to display the preprint in perpetuity. It is made available under aCC-BY-NC-ND 4.0 International license.

Primary- and volume-current contributions. We studied also the contributions of the primary and volume currents to the total magnetic field across the different sensor arrays. We defined TP as the ratio of the norms of the topographies of the total and primary current as

$$\mathrm{TP}_i = \frac{\|\mathbf{p}_i + \mathbf{v}_i\|}{\|\mathbf{p}_i\|} = \frac{\|\mathbf{t}_i\|}{\|\mathbf{p}_i\|}, \tag{14}$$

where $\mathbf{p}_i, \mathbf{v}_i$ and $\mathbf{t}_i$ denote the ith columns of the corresponding matrices $\mathbf{P}, \mathbf{V}$ and $\mathbf{L}$. Considering the values of TP, three different scenarios arise:

- $\mathrm{TP} < 1$: Volume-current field decreases the overall amplitude of the primary-current field.
- $\mathrm{TP} \approx 1$: Volume currents do not noticeably decrease or increase the overall amplitude of the primary-current field.
- $\mathrm{TP} > 1$: Volume-current field increases the overall amplitude of the primary-current field.

We also quantified the relative overall magnitude of the topographies of the primary and volume currents for the different sensor arrays by calculating the ratio of the norms of these field components

$$\mathrm{PV}_i = \frac{\|\mathbf{p}_i\|}{\|\mathbf{v}_i\|}. \tag{15}$$

In addition to these amplitude-based measures, we investigated the differences in the field shapes of primary and volume currents by computing the correlation coefficient (Eq. (10)) between their topographies; we denote these values of correlation coefficient as $\mathrm{CC}_{\mathrm{PV}}$.

Topography overlap. We calculated the correlation between the topography of the reference source and the topographies of all other sources in the source space using Eq. (10). By labeling those sources with considerable correlations (absolute value of $\mathrm{CC} \geq 0.9$), we estimated the peak position error (PPE) and cortical area (CA) of the reference source. PPE is the distance of the reference source to the center-of-mass of the highly-correlated sources. Smaller values of PPE mean that the correlated sources are scattered closer to the reference source. CA is the relative cortical area of the highly-correlated sources and quantifies the spread of the sources that exhibit similar topographies. PPE and CA are expressed as

$$\mathrm{PPE} = \left\| \vec{r}_{\mathrm{ref}} - \frac{\sum_i |\mathrm{CC}_i| \vec{r}_i}{\sum_i |\mathrm{CC}_i|} \right\| \tag{16}$$

$$\mathrm{CA} = \sum_i A_i, \tag{17}$$

where the sums are taken across the labeled sources, CC_i is the correlation coefficient between the topographies of the reference source and source i, $\vec{r}_i$ and $\vec{r}_{\mathrm{ref}}$ are the locations of source i and the reference source, respectively, and A_i is the relative cortical area associated with source i. PPE and CA have been previously used to assess differences in minimum-norm estimation (Stenroos and Hauk, 2013).

bioRxiv preprint doi: https://doi.org/10.1101/073585; this version posted September 5, 2016. The copyright holder for this preprint (which was not certified by peer review) is the author/funder, who has granted bioRxiv a license to display the preprint in perpetuity. It is made available under aCC-BY-NC-ND 4.0 International license.

Sensor lead fields. We quantified the effect of sensor orientation and distance from the scalp on its FOV; for each sensor, we calculated the relative cortical area (Eq. (17)) for which the lead-field amplitude of the sensor was more than half of the maximum amplitude. This metric quantifies the effective field of view (eFOV) of the sensor as it measures the area spanned by the sources that are most visible to the given sensor. In addition, to investigate dependencies in the FOVs of the sensors in the array, we calculated correlations between the lead fields of the sensors using Eq. (10). Then we computed the number of sensors whose lead fields had substantial correlations (absolute value of CC > 0.8) with the lead field of the reference sensor. This number can be considered as a rough measure of independent information in the sensor's signal: the smaller the number is, the more unique the lead field of the sensor is and thus the more independent information the sensor measures.

Total information. Previously, the performance of various MEG arrays has been assessed by computing the total information I_{tot} conveyed by the array (Kemppainen and Ilmoniemi, 1989; Nenonen et al., 2004; Schneiderman, 2014). I_{tot} quantifies all of the aspects of the forward-model-based metrics, e.g., sensor distances to the sources, sensor configuration, sensor type, SNR and dependencies of the sensor lead fields, with a single number. We also used this metric to evaluate the performance of the arrays.

We assume that the signal and the noise of a channel are independent and normally distributed; according to Shannon's theory of communication the information per sample of ith channel is then $I_i = \frac{1}{2}\log_2(\text{SNR}_i + 1)$, where SNR_i is the power signal-to-noise ratio of the channel (Shannon and Weaver, 1949). We further assume that the source time-series are uncorrelated and that their amplitudes follow Gaussian distribution: $j_i \sim \mathcal{N}(0, q^2)$, where q^2 assumes the same value as in Sec. 3.5; in addition, we only take into account the sensor noise. The SNR of channel i is $\text{SNR}_i = q^2||\tilde{\mathbf{l}}_i||^2$, where $\tilde{\mathbf{l}}_i$ is the ith row of the whitened lead-field matrix $\tilde{\mathbf{L}}$. With the assumption of a diagonal noise covariance matrix, SNR simplifies into $\text{SNR}_i = q^2\|\mathbf{l}_i\|^2/\sigma_i^2$.

To obtain the total information conveyed by the array by summing the contributions of individual channels, the sensor lead fields must be orthogonalized via an eigenvalue decomposition. First, we generate the matrix

$$\mathbf{M} = \tilde{\mathbf{L}}\tilde{\mathbf{L}}^T, \tag{18}$$

and compute its eigenvalue decomposition $\mathbf{M} = \mathbf{U}\mathbf{S}\mathbf{U}^T$, where the columns of $\mathbf{U}$ are the eigenvectors of $\mathbf{M}$ and $\mathbf{S}$ is a diagonal matrix with eigenvalues λ_j of $\mathbf{M}$ in the diagonal. The orthogonalized lead fields are then $\tilde{\mathbf{l}}'_i = (\mathbf{U}^T\tilde{\mathbf{L}})_i$ while the orthogonalized SNRs are $\text{SNR}'_i = q^2||(\mathbf{U}^T\tilde{\mathbf{L}})_i||^2$. The total information per sample of a multichannel system is then given by

$$I_{\text{tot}} = \frac{1}{2}\sum_{i=1}^{N_c}\log_2(\text{SNR}'_i + 1). \tag{19}$$

Point-spread functions. To evaluate the differences between the arrays in linear distributed-source estimation, we used metrics derived from the resolution matrix (Hauk et al., 2011; Liu et al., 2002; Molins et al., 2008; de Peralta Menendez et al., 1997; Stenroos and Hauk, 2013). Resolution matrix $\mathbf{K}$ gives the relation between the estimated and modeled current distributions as follows:

$$\tilde{\mathbf{j}} = \mathbf{G}\mathbf{b} = \mathbf{G}\mathbf{L}\mathbf{j} = \mathbf{K}\mathbf{j}. \tag{20}$$

The columns of $\mathbf{K}$ are PSFs and they describe how a point source is distorted by the imaging system. By replacing CC in Eqs. (16) and (17) by PSF and picking the indices for which $|\text{PSF}_i| \geq$

bioRxiv preprint doi: https://doi.org/10.1101/073585; this version posted September 5, 2016. The copyright holder for this preprint (which was not certified by peer review) is the author/funder, who has granted bioRxiv a license to display the preprint in perpetuity. It is made available under aCC-BY-NC-ND 4.0 International license.

$0.5 \times \mathrm{PSF}_{\mathrm{max}}$, we can quantify the accuracy of a sensor array in minimum-norm estimation with PPE and CA; PPE quantifies the localization accuracy while CA estimates the spread of the PSF.

4. Results

4.1. Verifications

For one subject, the average relative errors (REs) between the topographies of the sources computed with coarser and denser BEM meshes are 0.27%, 0.33% and 0.18% for nOPM, tOPM and mSQUID, respectively, while the 95th percentiles are 0.71%, 0.87% and 0.54%. The histograms of the values of correlation coefficient (CC) are strongly peaked at 1 for nOPM, tOPM and mSQUID as the 2.5th percentiles were over 0.999 for all the arrays.

The percentiles for one subject's REs and CCs for different skull conductivities (using the topography with conductivity of 0.33/25 S/m as the reference) are shown in Table 2. The histograms of RE and CC between nOPM, tOPM and mSQUID are highly similar.

Table 2: The 2.5th, 25th, 50th, 75th and 97.5th percentiles for the relative errors (REs) and correlation coefficients (CCs) between the topographies computed with different skull conductivity values for one subject. Topographies with skull conductivity of 0.33/25 S/m were used as the reference, and the skull conductivity was set to 0.33/K S/m for the test topographies. The values that are higher than 0.999 are denoted with an asterisk.

	K	nOPM	tOPM	mSQUID
RE (%)	50	(0.4 0.7 1.0 2.0 6.4)	(0.4 0.7 1.1 2.1 7.0)	(0.3 0.6 1.0 1.9 6.3)
	80	(0.6 1.0 1.5 3.0 9.4)	(0.7 1.1 1.6 3.2 10.2)	(0.5 0.9 1.4 2.8 9.2)
CC	50	(0.999, ∗,∗,∗,∗)	(0.998, ∗,∗,∗,∗)	(0.999, ∗,∗,∗,∗)
	80	(0.997, ∗,∗,∗,∗)	(0.996, ∗,∗,∗,∗)	(0.997, ∗,∗,∗,∗)

4.2. Forward metrics

The relative sensitivities for different combinations of nOPM, tOPM and mSQUID arrays are illustrated in Fig. 2. On average, the topography powers of the nOPM and tOPM are 7.5 and 5.3 times higher than the topography power of mSQUID. The topography powers of the OPM arrays vs. mSQUID are still higher for the superficial sources ($\sim$9.4 for nOPM and $\sim$7.1 for tOPM) and decrease for deeper sources ($\sim$6.5 for nOPM and $\sim$4.5 for tOPM). The topography power of the nOPM array is on average 1.5 times higher than that of tOPM, and it is higher for almost every point of the source space.

The comparisons of the primary- and volume-current components of the topographies are displayed in Fig. 3. The overall amplitudes of the volume current topographies are of the same magnitude as those of the primary currents for tOPM as the values of PV are concentrated around one. The field due to volume currents substantially suppresses the overall amplitude of the primary-current topography in tangential measurements since TP $\ll 1$ for tOPM (mean 0.28, range 0.05–0.46). For nOPM and mSQUID, the overall magnitude of the primary current topography is much higher than that of volume currents, as the majority of PV $\gg 1$. Additionally, volume currents do not result in a major decrease in the overall amplitude of primary current topography in nOPM and mSQUID arrays as the values of TP are closer to one (mean 0.90 and 0.85 for nOPM and mSQUID, respectively). Volume currents increase the visibility of some deep sources in particular when measuring with nOPM and mSQUID arrays (regions where TP > 1). Furthermore, the closer the normal-component measuring sensors are to the sources, the larger

bioRxiv preprint doi: https://doi.org/10.1101/073585; this version posted September 5, 2016. The copyright holder for this preprint (which was not certified by peer review) is the author/funder, who has granted bioRxiv a license to display the preprint in perpetuity. It is made available under aCC-BY-NC-ND 4.0 International license.

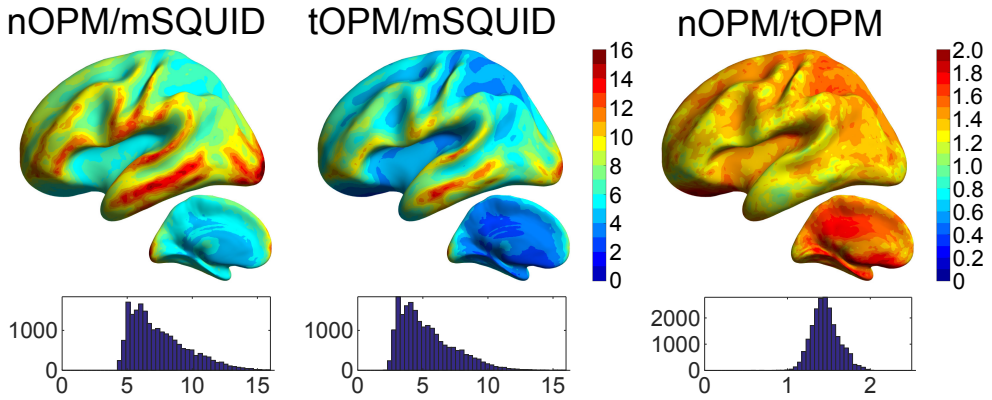

Figure 2: The relative sensitivities of the different arrays. Only the left hemisphere is shown but the histograms include values for both hemispheres.

the overall magnitude of the primary-current topography is relative to the volume-current topography since the mean and range of PV are 3.41 and 0.71–6.41 for nOPM and 2.67 and 0.62–4.81 for mSQUID. As the majority of the CC_{PV} values are well below zero, the volume-current topographies tend to have the opposite shape to the primary-current topographies. For tOPM, the correlation coefficients are very close to –1, i.e., exactly opposite topographical shape of the volume currents compared to the primary currents. The average CC_{PV} for nOPM, tOPM and mSQUID is –0.44, –0.95 and –0.53 while the ranges are –0.94–0.23, –1.0–(–0.89) and –0.97–0.17, respectively.

Fig. 4 shows the peak position error (PPE) and cortical area (CA), which were based on correlations between the source topographies. CA is clearly smaller for nOPM, tOPM and gSQUID than for mSQUID, indicating that the topographies of the sources show less overlap in OPM and SQUID-gradiometer arrays. PPE is also smaller for the nOPM, tOPM and gSQUID suggesting that the similar-topography sources are closer to the actual source for these arrays. The measures are similar between nOPM, tOPM and gSQUID. The averages for PPE are 0.51, 0.45, 0.79 and 0.52 cm and for CA they are 0.26%, 0.19%, 0.66% and 0.26% for nOPM, tOPM, mSQUID and gSQUID, respectively.

The computed eFOVs of the sensors are illustrated in Fig. 5 as histograms into which the values from all subjects were pooled. The same figure also shows the number of sensors with substantial lead-field correlations (absolute value of $CC > 0.8$) with the reference sensor. When the magnetometers are brought closer to the scalp, their FOV shrinks as the values of eFOV are, on average, smaller for nOPM and tOPM than for mSQUID. Additionally, the eFOVs in tOPM are more focal than those in nOPM. The SQUID gradiometers also show smaller FOVs than the SQUID magnetometers. The eFOVs of gSQUID are similar to those of nOPM and tOPM. The mean values of eFOVs are 0.69%, 0.25%, 3.02% and 0.53% for nOPM, tOPM, mSQUID and gSQUID, respectively. As the plots on the right side of the Fig. 5 illustrate, the numbers of lead-field-correlated ($CC > 0.8$) sensors are evidently smaller in the on-scalp OPM arrays. By pooling the data across the subjects, we found that the median values of the lead-field-correlated sensors are 0, 1, 4 and 2 for the nOPM, tOPM, mSQUID and gSQUID, respectively.

The total information capacities of the arrays are presented in Fig. 6. Across the subjects, mSQUID and gSQUID convey similar amount of information: the averages are 413 and 383 bits

bioRxiv preprint doi: https://doi.org/10.1101/073585; this version posted September 5, 2016. The copyright holder for this preprint (which was not certified by peer review) is the author/funder, who has granted bioRxiv a license to display the preprint in perpetuity. It is made available under aCC-BY-NC-ND 4.0 International license.

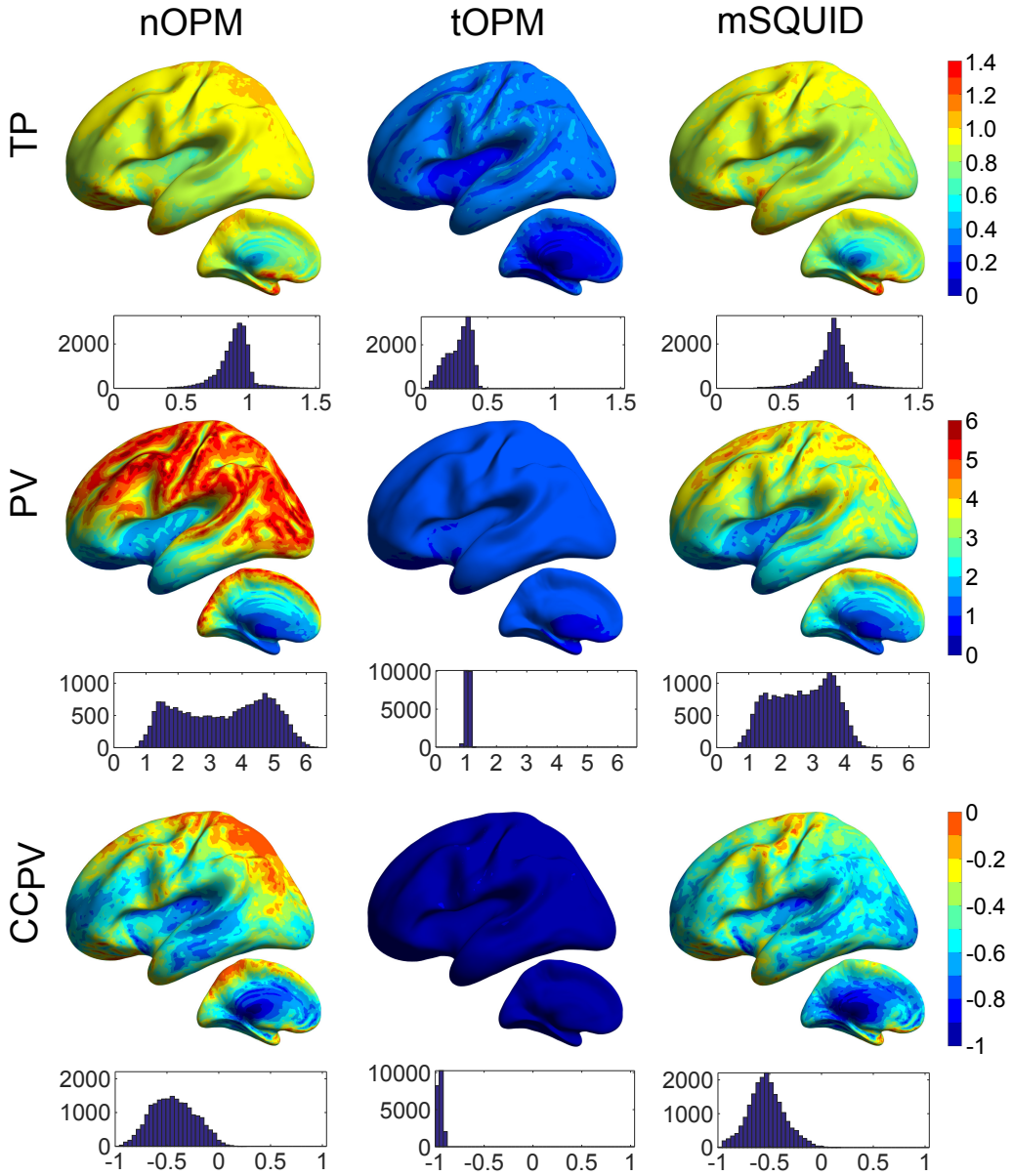

Figure 3: The ratios of the norms of the topographies of the total and primary current TP, the ratios of the norms of primary- and volume-current topographies PV, and the correlation coefficient between the topographies of the primary and volume currents (CC_{PV}). Only the left hemisphere is shown but the histograms include values for both hemispheres.

bioRxiv preprint doi: https://doi.org/10.1101/073585; this version posted September 5, 2016. The copyright holder for this preprint (which was not certified by peer review) is the author/funder, who has granted bioRxiv a license to display the preprint in perpetuity. It is made available under aCC-BY-NC-ND 4.0 International license.

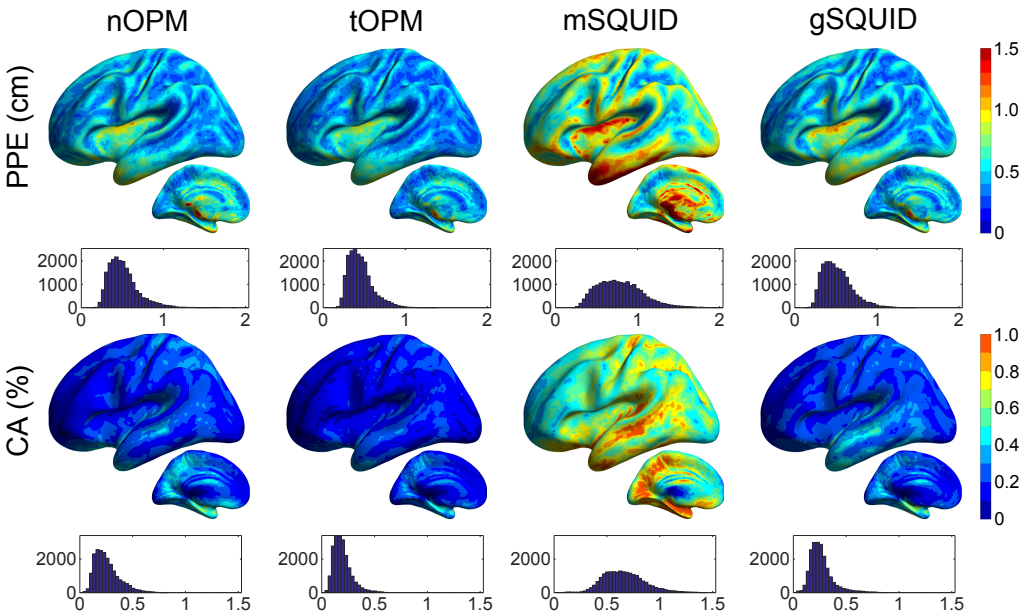

Figure 4: Peak position error (PPE) and cortical area (CA) computed from the correlation coefficients between the topographies. Only the left hemisphere is shown but the histograms include values for both hemispheres.

per sample, respectively. Combining mSQUID and gSQUID to aSQUID increases the average information to 506 bits per sample. Both of the OPM arrays (nOPM and tOPM) provide more information than the aSQUID. tOPM yields more information than nOPM. The combination array aOPM carries even more information than its sub-arrays nOPM and tOPM. The averages of the total information across the subjects are 656, 939 and 1307 bits per sample for nOPM, tOPM and aOPM, respectively.

4.3. Point-spread functions

The results for the PSF-based metrics are displayed in Fig. 7 for nOPM, tOPM, aOPM, mSQUID and aSQUID arrays. Cortical maps and histograms of PPE between the different arrays exhibit similarities; yet, differences are evident in CA. Comparison between the normal-component-measuring arrays indicates that PSFs are less spread in nOPM: CA is larger for every source for mSQUID; the averages of CA are 0.67% and 1.57% for nOPM and mSQUID, respectively. The spread of the PSF does not necessarily correlate with the localization accuracy as the PPE of nOPM is larger for 60% of the sources. The averages of PPE are 1.30 and 1.27 cm for nOPM and mSQUID, respectively. For the most superficial sources the PPE is smaller in nOPM: averages of the PPE for the most superficial sources of left hemisphere are 0.48 cm for nOPM and 0.56 cm for mSQUID.

The results between nOPM and tOPM are similar; averages of PPE and CA for tOPM are 1.31 cm and 0.64% while average PPE is 0.46 cm for superficial sources. For aOPM, the localization accuracy is slightly enhanced compared to the individual arrays, especially for the superficial sources. Averages of PPE and CA for aOPM are 1.26 cm and 0.57% for all sources while for the superficial sources the average PPE is 0.40 cm.

bioRxiv preprint doi: https://doi.org/10.1101/073585; this version posted September 5, 2016. The copyright holder for this preprint (which was not certified by peer review) is the author/funder, who has granted bioRxiv a license to display the preprint in perpetuity. It is made available under aCC-BY-NC-ND 4.0 International license.

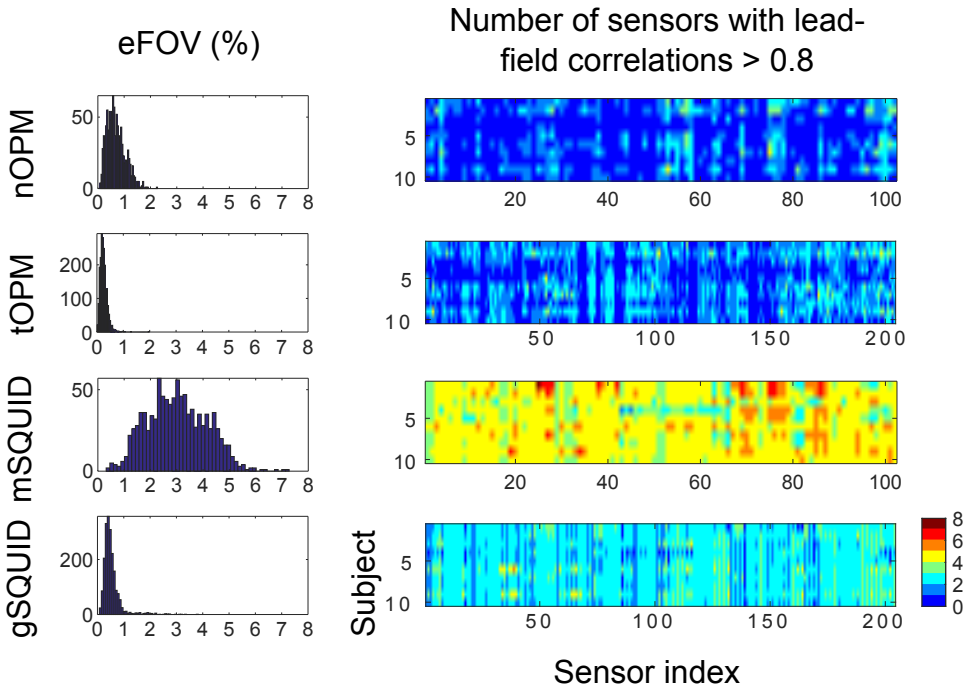

Figure 5: The effective field of view (eFOV) of the sensors, and the number of sensors with substantial lead-field correlations. Left: Histograms of eFOV with values from different subjects pooled. Right: Plots displaying the number of sensors whose lead fields had a correlation coefficient larger than 0.8 with the lead field of the given sensor. Each row represents data from one subject.

bioRxiv preprint doi: https://doi.org/10.1101/073585; this version posted September 5, 2016. The copyright holder for this preprint (which was not certified by peer review) is the author/funder, who has granted bioRxiv a license to display the preprint in perpetuity. It is made available under aCC-BY-NC-ND 4.0 International license.

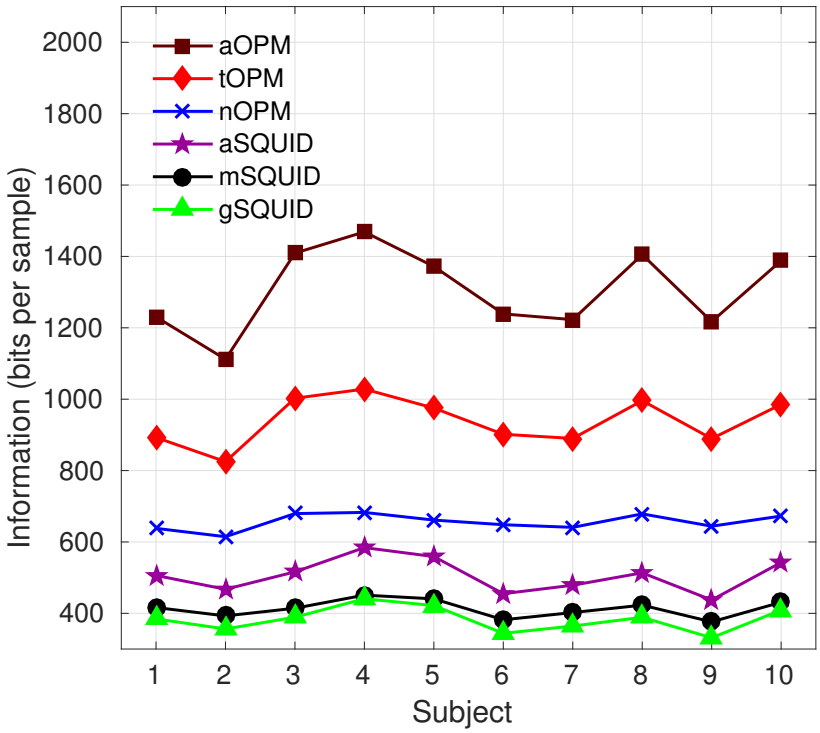

Figure 6: The total information capacities of the arrays derived from the Shannon's theory of communication.

bioRxiv preprint doi: https://doi.org/10.1101/073585; this version posted September 5, 2016. The copyright holder for this preprint (which was not certified by peer review) is the author/funder, who has granted bioRxiv a license to display the preprint in perpetuity. It is made available under aCC-BY-NC-ND 4.0 International license.

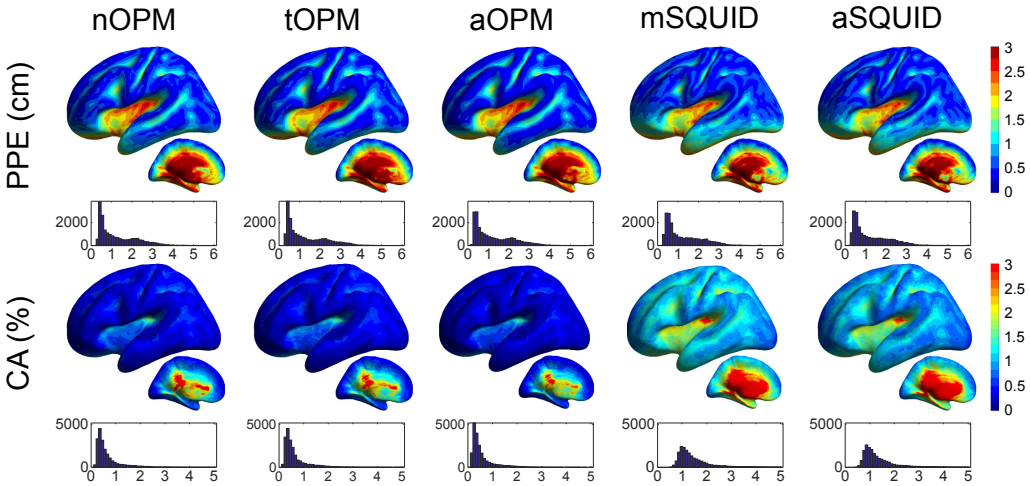

Figure 7: Peak position error (PPE) and cortical area (CA) computed from the point spread functions. Only the left hemisphere is shown but the histograms include data for both hemispheres.

Comparison of the OPM arrays to the 306-channel SQUID system shows that there is a substantial decrease of the PSF spread for all OPM arrays while the localization performance (PPE) is similar. Nonetheless, for superficial sources the localization accuracy of aOPM is better than that of aSQUID; for superficial sources the average PPE of aSQUID is 0.53 cm. The averages of PPE and CA of aSQUID are 1.26 cm and 1.45%.

5. Discussion

The aim of this study was to assess the possible benefits of on-scalp MEG arrays that can be constructed using novel magnetic field sensors, e.g., optically-pumped magnetometers or high-T_c SQUIDs. The assessment was done by comparing MEG sensor arrays (mSQUID: 102 magnetometers; gSQUID: 204 planar gradiometers; aSQUID: combination of mSQUID and gSQUID) with hypothetical OPM arrays that measured normal (nOPM; 102 sensors), tangential (tOPM; 204 sensors) or all components (aOPM; 306 sensors) of the magnetic field. In the comparison, we used metrics derived from both forward and inverse models that quantified signal power, information, similarity of source topographies, overlap of the sensor lead fields, localization accuracy and resolution. Although we refer to the on-scalp sensors as OPMs, the results are applicable to any kind of sensor with similar characteristics.

Recently, Boto and colleagues (2016) reported a simulation study where they investigated the performance of on-scalp MEG sensor arrays. In the simulations, they employed a SQUID sensor configuration of the 275-channel CTF MEG system and determined the OPM sensor positions by projecting the SQUID locations to 4 mm from scalp. In that study, the authors focused on the spatial resolution and reconstruction accuracy in beamforming whereas we based our resolution analysis on the topography correlations (and thereby only on the physics) without making reference to any particular inversion method. In the following, we compare our results to theirs whenever possible.

bioRxiv preprint doi: https://doi.org/10.1101/073585; this version posted September 5, 2016. The copyright holder for this preprint (which was not certified by peer review) is the author/funder, who has granted bioRxiv a license to display the preprint in perpetuity. It is made available under aCC-BY-NC-ND 4.0 International license.

5.1. Sensitivity

Among the nOPM, tOPM, and mSQUID arrays, nOPM had the strongest overall topography power despite that the number of sensors in tOPM was double and the topography powers were not normalized by the sensor count. Assuming noise levels of 6 and 3 $\mathrm{fT}/\sqrt{\mathrm{Hz}}$ for OPM and SQUID magnetometers, respectively, the relative sensitivities transform into overall SNR gain of 1.9 for nOPM compared to mSQUID, while this figure is 0.7 for tOPM. For sources in the superficial parts of the brain, the average SNR of nOPM and tOPM are 2.4 and 0.9 times that of mSQUID. On the other hand, for equal overall SNR between the OPM and mSQUID arrays, the sensor noise levels should be 8.2 and 4.9 $\mathrm{fT}/\sqrt{\mathrm{Hz}}$ for nOPM and tOPM, respectively.

In their sensitivity analysis, Boto and colleagues (2016) assumed that OPMs and SQUIDs have an equal noise level of 10 $\mathrm{fT}/\sqrt{\mathrm{Hz}}$; they reported fivefold improvement in average (amplitude) SNR of the OPM array compared to the SQUID array. The corresponding average (power) SNR gain we attained was 7.5 (relative sensitivity between nOPM and mSQUID). A few factors may explain these differences: first, Boto and colleagues had more sensors (275 vs. 102) as well as different sensor models and distances from the scalp. Second, they used the multiple local spheres head model (Huang et al., 1999) in the forward computation which is less realistic than the three-shell BEM we employed (Stenroos et al., 2014).

Our results suggest that in tOPM measurements, the field due to volume currents screens the field of the primary current much more than in the normal-component measurements. While the volume-current field is present also in the normal component, its effect is much more drastic in measurements of the tangential component. Thus, measuring and modeling tangential field components is likely more sensitive to errors and simplifications in volume conductor models. In addition, since the relative primary-current contribution further increases when the normal-component-measuring sensors are brought closer to the scalp, these sensors appear the optimal choice for on-scalp measurements.

5.2. Correlation metrics

The measures based on correlations between the source topographies showed that the OPM arrays offer clear benefits over SQUID magnetometers when it comes to the topography overlap: the OPM arrays exhibit less-correlated topographies, and the correlated sources are closer to the actual sources which generate the topographies. In addition, these measures were slightly smaller (better) for the tOPM than for the nOPM, which can be due to the larger number of sensors in tOPM; more sensors allow more possibilities for the topographies to deviate from each other. The measures were smaller for gSQUID compared to mSQUID, showing the benefit of the focal sensitivity of planar gradiometers. In addition, the measures were similar between gSQUID and OPM arrays. Future studies could investigate whether the topography correlations can be further reduced by gradiometrization of OPMs.

The on-scalp OPMs showed more focal fields-of-view than the traditional SQUID magnetometers. Furthermore, the tangential vs. normal OPMs have more focal lead fields. The planar gradiometers also have smaller FOVs than the magnetometers at the same distance from the scalp; values of eFOV for gSQUID are of the same order as for the OPMs. As the OPMs have small FOVs, the OPM arrays could be constructed such that the FOVs of the individual sensors would overlap as little as possible while maximizing the number of sensors on the scalp. Such an array could minimize "field spread" (the interdependencies of sensor signals) which would be particularly beneficial for functional connectivity analysis in the sensor space (see Schoffelen and Gross (2009)). Additionally, minimizing the lead-field overlap would also improve the

bioRxiv preprint doi: https://doi.org/10.1101/073585; this version posted September 5, 2016. The copyright holder for this preprint (which was not certified by peer review) is the author/funder, who has granted bioRxiv a license to display the preprint in perpetuity. It is made available under aCC-BY-NC-ND 4.0 International license.

interpretability of sensor-level data. The benefits of lead-field-overlap minimization to source-localization performance are not that evident and could be studied further. The OPM arrays had less lead-field-correlated sensors than gSQUID and mSQUID. Further, the numbers of lead-field-correlated sensors in nOPM and tOPM were similar, though it should be taken into account that the tOPM array comprises twice the number of sensors.

5.3. Total information and point spread

According to our results, the information capacities of the OPM arrays are clearly higher than that of the state-of-the-art SQUID array. In addition, the tOPM array with 204 sensors conveys more information than the nOPM array with 102 sensors, which can be attributed to the larger number of sensors in tOPM; we verified that the measurement of only one tangential component (longitudinal or latitudinal) at 102 locations does not yield more information than the measurement of the normal component.

Furthermore, our results clearly indicate that the normal and tangential components carry independent information as the information capacity of the aOPM is higher than the information capacities of its sub-arrays nOPM and tOPM, addressing the question of redundancy of these measurements (de Munck and Daffertshofer, 2012). Similar observations have been made for cardiomagnetic fields (Arturi et al., 2004).

Our total information analysis also provides a useful simulation benchmark. To facilitate the comparison of different sensor arrays, the source amplitudes can be set such that the average SNR across the sources for the SQUID magnetometers of the Elekta MEG system is one. Then, the SQUID magnetometers can be taken as a reference and metrics computed for other arrays using the same source amplitudes.

The results from the PSF analysis showed that localization accuracies of the OPM and SQUID arrays in minimum-norm estimation are similar. However, the OPM arrays provided substantially more focal point-spread functions and thus should offer higher spatial resolution.

5.4. Models and field computation

When magnetic fields are evaluated at points close to the BEM surfaces, the coarseness of the meshes could affect the results. However, our verification suggest that meshes with 2 562 vertices (average sidelength of 7 mm) with a linear Galerkin BEM are sufficient for the OPM arrays. Additionally, the sensitivities of the topographies to the densities of the BEM surface tesselations are of the same order of magnitude for OPM and SQUID arrays.

In this study, we used anatomical models produced by the standard pipeline of the MNE software that employs the watershed algorithm for surface segmentation. In future studies, simulations could be extended to benefit from more accurate tissue-boundary reconstructions (Stenroos and Nummenmaa, 2016; Vorwerk et al., 2014).

The value of skull conductivity affects the solutions as it determines the amount of volume current 'allowed' to flow in the skull and scalp compartments. We used the value 0.33/25 S/m and tested the sensitivity of the computed topographies to skull conductivity by comparing them to topographies with skull conductivity values of 0.33/50 and 0.33/80 S/m. We found that the shapes and amplitudes of the topographies were generally robust against this conductivity. Yet, skull conductivity may affect the amplitudes of some low-SNR sources (deep sources) at the sensors. In summary, we conclude that three-shell forward models for the OPM arrays are not more sensitive to skull conductivity errors than those for SQUID arrays.

We also briefly compared topographies obtained with linear collocation (LC) and linear Galerkin (LG) BEM. The average REs between topographies computed using LC and LG BEM

bioRxiv preprint doi: https://doi.org/10.1101/073585; this version posted September 5, 2016. The copyright holder for this preprint (which was not certified by peer review) is the author/funder, who has granted bioRxiv a license to display the preprint in perpetuity. It is made available under aCC-BY-NC-ND 4.0 International license.

were 0.4% and 3.8% for nOPM and tOPM, respectively. Thus, field computation for normal-component-measuring OPMs could be done with freely available BEM solvers (such as one provided by Stenroos et al. (2014)), while OPMs that measure tangential components may require more accurate BEM solvers.

The sensing volume of an OPM sensor was modeled as a (5-mm)^3 cube with eight integration points while the SQUID models were based on those in the MNE software. We assumed a noise level of 6 fT/ $\sqrt{\text{Hz}}$ for the OPM sensor based on the work by Shah and Wakai (2013) who reported such a field resolution for their sensor in optimal conditions. Their sensor comprised a (4-mm)^3 vapor cell, which is roughly equal to the sensitive volume in our OPM model. For the SQUID magnetometers and gradiometers, we assumed sensor noise levels of 3 fT/ $\sqrt{\text{Hz}}$ and 3 fT/cm $\sqrt{\text{Hz}}$, which are typical values for the Elekta Neuromag® MEG systems.

5.5. Normal vs. tangential sensors

MEG devices have traditionally comprised normal-component-measuring sensors. Switching to a tangential array would introduce a profound change in the interpretation of the sensor-level data; e.g. the isocontours would look very different. In addition, compared to normal-component measurements, the higher sensitivity of tangential measurements to volume currents might necessitate more accurate head models and numerical methods. For the same reason, individual differences in the conductivity profile of the head would render comparisons of sensor-level data between individuals less accurate. Further, to obtain similar SNRs, the requirements for the sensor noise level are more strict for tangential sensors due to their lower topography power. For these reasons, we consider the normal-component-measuring sensors to be the optimal choice for MEG.

6. Conclusions

We examined the performance of hypothetical on-scalp MEG arrays compared to a current state-of-the-art MEG system. The results indicate that on-scalp arrays should offer clear benefits over traditional SQUID arrays in several aspects of performance; signal-to-noise ratio, total information conveyed by the array, and the achievable spatial resolution should improve substantially. These measures can be used to guide the design of on-scalp MEG arrays for optimal performance.

7. Acknowledgements

The authors thank Dr. Jukka Nenonen for comments on the manuscript, Advanced Magnetic Imaging centre of Aalto Neuroimaging Infrastructure for the MR-images, and Aalto University Science-IT for providing computational resources. Research reported in this publication was supported by the European Union FP7 project “Magnetrodes” (grant number 600730) and by the National Institute Of Neurological Disorders And Stroke of the National Institutes of Health under Award Number R01NS094604. The content is solely the responsibility of the authors and does not necessarily represent the official views of the funding organizations.

bioRxiv preprint doi: https://doi.org/10.1101/073585; this version posted September 5, 2016. The copyright holder for this preprint (which was not certified by peer review) is the author/funder, who has granted bioRxiv a license to display the preprint in perpetuity. It is made available under aCC-BY-NC-ND 4.0 International license.

References

Allred, J., Lyman, R., Kornack, T., and Romalis, M. (2002). High-sensitivity atomic magnetometer unaffected by spin-exchange relaxation. *Physical Review Letters*, 89(13):130801.

Arturi, C. M., Di Rienzo, L., and Haueisen, J. (2004). Information content in single-component versus three-component cardiomagnetic fields. *Magnetics, IEEE Transactions on*, 40(2):631–634.

Boto, E., Bowtell, R., Krüger, P., Fromhold, T. M., Morris, P. G., Meyer, S. S., Barnes, G. R., and Brookes, M. J. (2016). On the potential of a new generation of magnetometers for meg: A beamformer simulation study. *PLoS ONE*, 11(8):1–24.

Budker, D. and Kimball, D. F. J. (2013). *Optical magnetometry*. Cambridge University Press.

Budker, D. and Romalis, M. (2007). Optical magnetometry. *Nature Physics*, 3(4):227–234.

Dale, A. M., Fischl, B., and Sereno, M. I. (1999). Cortical surface-based analysis: I. Segmentation and surface reconstruction. *NeuroImage*, 9(2):179–194.

Dale, A. M. and Sereno, M. I. (1993). Improved localizadon of cortical activity by combining EEG and MEG with MRI cortical surface reconstruction: A linear approach. *Journal of Cognitive Neuroscience*, 5(2):162–176.

de Munck, J. C. and Daffertshofer, A. (2012). Radial and tangential components of dipolar sources and their magnetic fields. *Clinical Neurophysiology*, 123(8):1477–1478.

de Peralta Menendez, R. G., Hauk, O., Gonzalez-Andino, S., Vogt, H., and Michel, C. (1997). Linear inverse solutions with optimal resolution kernels applied to electromagnetic tomography. *Human Brain Mapping*, 5(6):454–467.

Fischl, B. (2012). Freesurfer. *NeuroImage*, 62(2):774–781.

Fischl, B., Sereno, M. I., and Dale, A. M. (1999a). Cortical surface-based analysis: II: Inflation, flattening, and a surface-based coordinate system. *NeuroImage*, 9(2):195–207.

Fischl, B., Sereno, M. I., Tootell, R. B., Dale, A. M., et al. (1999b). High-resolution intersubject averaging and a coordinate system for the cortical surface. *Human Brain Mapping*, 8(4):272–284.

Geselowitz, D. B. (1970). On the magnetic field generated outside an inhomogeneous volume conductor by internal current sources. *Magnetics, IEEE Transactions on*, 6(2):346–347.

Goldenholz, D. M., Ahlfors, S. P., Hämäläinen, M. S., Sharon, D., Ishitobi, M., Vaina, L. M., and Stufflebeam, S. M. (2009). Mapping the signal-to-noise-ratios of cortical sources in magnetoencephalography and electroencephalography. *Human Brain Mapping*, 30(4):1077–1086.

Gramfort, A., Luessi, M., Larson, E., Engemann, D. A., Strohmeier, D., Brodbeck, C., Parkkonen, L., and Hämäläinen, M. S. (2014). MNE software for processing MEG and EEG data. *NeuroImage*, 86:446–460.

Hämäläinen, M., Hari, R., Ilmoniemi, R. J., Knuutila, J., and Lounasmaa, O. V. (1993). Magnetoencephalography–theory, instrumentation, and applications to noninvasive studies of the working human brain. *Reviews of Modern Physics*, 65(2):413.

Hämäläinen, M. S. and Ilmoniemi, R. (1994). Interpreting magnetic fields of the brain: minimum norm estimates. *Medical & Biological Engineering & Computing*, 32(1):35–42.

Hauk, O., Wakeman, D. G., and Henson, R. (2011). Comparison of noise-normalized minimum norm estimates for MEG analysis using multiple resolution metrics. *NeuroImage*, 54(3):1966–1974.

Huang, M., Mosher, J., and Leahy, R. (1999). A sensor-weighted overlapping-sphere head model and exhaustive head model comparison for MEG. *Physics in Medicine and Biology*, 44(2):423.

Johnson, C., Schwindt, P. D., and Weisend, M. (2010). Magnetoencephalography with a two-color pump-probe, fiber-coupled atomic magnetometer. *Applied Physics Letters*, 97(24):243703.

Kemppainen, P. and Ilmoniemi, R. (1989). Channel capacity of multichannel magnetometers. In *Advances in Biomagnetism*, pages 635–638. Springer.

Lin, F.-H., Belliveau, J. W., Dale, A. M., and Hämäläinen, M. S. (2006a). Distributed current estimates using cortical orientation constraints. *Human Brain Mapping*, 27(1):1–13.

Lin, F.-H., Witzel, T., Ahlfors, S. P., Stufflebeam, S. M., Belliveau, J. W., and Hämäläinen, M. S. (2006b). Assessing and improving the spatial accuracy in MEG source localization by depth-weighted minimum-norm estimates. *NeuroImage*, 31(1):160–171.

Liu, A. K., Dale, A. M., and Belliveau, J. W. (2002). Monte carlo simulation studies of EEG and MEG localization accuracy. *Human Brain Mapping*, 16(1):47–62.

Mhaskar, R., Knappe, S., and Kitching, J. (2012). A low-power, high-sensitivity micromachined optical magnetometer. *Applied Physics Letters*, 101(24):241105.

Molins, A., Stufflebeam, S. M., Brown, E. N., and Hämäläinen, M. S. (2008). Quantification of the benefit from integrating MEG and EEG data in minimum l_2-norm estimation. *NeuroImage*, 42(3):1069–1077.

Nenonen, J., Kajola, M., Simola, J., and Ahonen, A. (2004). Total information of multichannel MEG sensor arrays. In *Proceedings of the 14th International Conference on Biomagnetism (Biomag2004)*, pages 630–631.

Öisjöen, F., Schneiderman, J. F., Figueras, G., Chukharkin, M., Kalabukhov, A., Hedström, A., Elam, M., and Winkler,

bioRxiv preprint doi: https://doi.org/10.1101/073585; this version posted September 5, 2016. The copyright holder for this preprint (which was not certified by peer review) is the author/funder, who has granted bioRxiv a license to display the preprint in perpetuity. It is made available under aCC-BY-NC-ND 4.0 International license.

D. (2012). High-T_c superconducting quantum interference device recordings of spontaneous brain activity: Towards high-T_c magnetoencephalography. *Applied Physics Letters*, 100(13):132601.

Plonsey, R. and Heppner, D. B. (1967). Considerations of quasi-stationarity in electrophysiological systems. *The Bulletin of Mathematical Biophysics*, 29(4):657–664.

Schneiderman, J. F. (2014). Information content with low-vs. high-T_c SQUID arrays in MEG recordings: The case for high-T_c SQUID-based MEG. *Journal of Neuroscience Methods*, 222:42–46.

Schoffelen, J.-M. and Gross, J. (2009). Source connectivity analysis with MEG and EEG. *Human Brain Mapping*, 30(6):1857–1865.

Ségonne, F., Dale, A., Busa, E., Glessner, M., Salat, D., Hahn, H., and Fischl, B. (2004). A hybrid approach to the skull stripping problem in MRI. *NeuroImage*, 22(3):1060–1075.

Shah, V. K. and Wakai, R. T. (2013). A compact, high performance atomic magnetometer for biomedical applications. *Physics in Medicine and Biology*, 58(22):8153.

Shannon, C. E. and Weaver, W. (1949). The mathematical theory of communication. *University of Illinois Press, Urbana*.

Stenroos, M. and Hauk, O. (2013). Minimum-norm cortical source estimation in layered head models is robust against skull conductivity error. *NeuroImage*, 81:265–272.

Stenroos, M., Hunold, A., and Haueisen, J. (2014). Comparison of three-shell and simplified volume conductor models in magnetoencephalography. *NeuroImage*, 94:337–348.

Stenroos, M., Mäntynen, V., and Nenonen, J. (2007). A Matlab library for solving quasi-static volume conduction problems using the boundary element method. *Computer Methods and Programs in Biomedicine*, 88(3):256–263.

Stenroos, M. and Nummenmaa, A. (2016). Incorporating and compensating cerebrospinal fluid in surface-based forward models of magneto- and electroencephalography. *PLoS ONE*, 11(7):1–23.

Stenroos, M. and Sarvas, J. (2012). Bioelectromagnetic forward problem: isolated source approach revis(it)ed. *Physics in Medicine and Biology*, 57(11):3517.

Vorwerk, J., Cho, J.-H., Rampp, S., Hamer, H., Knösche, T. R., and Wolters, C. H. (2014). A guideline for head volume conductor modeling in EEG and MEG. *NeuroImage*, 100:590–607.